Influence of Product Adsorption on the Operation of a Reverse-Flow Reactor

Rohit Garg, Abdul Garayhi, and Dan Luss
Dept. of Chemical Engineering, University of Houston, Houston, TX 77204

The adsorption on the catalyst surface of the product of an exothermic reaction in a reverse-flow reactor (RFR) may lead to large variations in the temporal effluent product concentration. Using a dilute reactant feed, the adsorbed product effluent concentration is low following each flow reversal, but it eventually exceeds the feed reactant concentration. The product adsorption may decrease the range of operating conditions (parameter values) for which the RFR can attain an ignited state. A cooled RFR may attain, for certain parameter values, complex dynamic states such as quasi-periodic and chaotic states. An increase in the adsorption capacity of the catalyst decreases the range of parameter values for which complex dynamic states exist. The desired period-1 operation of the RFR is more robust in the presence of product adsorption. Product adsorption may lead to surprising dynamic features, such as the coexistence of up to three stable quasi-periodic states for the same operating conditions.

Introduction

The reverse-flow reactor (RFR) has attracted much attention in recent years and comprehensive reviews of its operation were presented by Matros and Bunimovich (1996) and Kolios et al. (2000). The main applications of the RFR are destruction of pollutants such as volatile organic compounds present in low concentrations and carrying out exothermic reversible reactions, such as SO_2-oxidation (Boreskov and Matros, 1983; Nieken et al., 1994; van de Beld, 1995). Various attempts have been made to couple exothermic and endothermic reactions in an RFR (Snyder and Subramaniam, 1994; Kolios and Eigenberger, 1999) but none has led so far to a commercial process. Several attempts at using of an RFR for selective catalytic reduction of NO_x by ammonia have been reported (Agar and Ruppel, 1988; Noskov et al., 1996; Snyder and Subramaniam, 1998). This application of the RFR as a chromatographic reactor hinges on its ability to strongly adsorb the ammonia. Bunimovich et al. (1995) have shown that product adsorption during the oxidation of SO_2 may have a strong impact on the transient behavior of an RFR. When an exothermic reaction is carried out in an RFR, following a flow reversal the moving hot zone may desorb the adsorbed reactant from the cold reactor section, decreasing the overall conversion. Such a deleterious reactant desorption was observed by van de Beld et al. (1994) during methanol oxidation.

Heat losses and/or cooling of the RFR may lead to rather complex dynamic behavior of an RFR, as shown by Khinast et al. (1998, 1999). We report here a study of the operation of a cooled RFR in which the irreversible exothermic reaction $A \rightarrow P$ is carried out and the product P is adsorbed on the catalyst. We examine the behavioral features of this operation and the associated dynamic features. This information provides insight and guidance to finding the optimal mode of operation.

Mathematical Model of the Reactor

We consider a single irreversible, exothermic, first-order reaction $A \rightarrow P$ carried out in an RFR in which the flow direction is reversed periodically. The product P is adsorbed on the catalyst support. We describe the reactor by a one-dimensional pseudohomogeneous model (Vortmeyer and Schaefer, 1974). It was shown that the differences between the predictions of the heterogeneous and pseudohomogeneous models are usually rather small (Khinast et al., 1999). Our model accounts for axial heat and mass dispersion and external mass-transfer resistance between the fluid and the catalyst. We assume that the feed is a dilute mixture of the

Correspondence concerning this article should be addressed to D. Luss.
Present address of A. Garayhi: Linde AG, Werksgruppe VA, Abt. CVO, Dr.-Carl-v.-Linde-Str. 6-14, 82049 Hoellriegelskreuth, Germany.

reactant so that product adsorption does not affect the velocity in the reactor. We ignore the pressure variation along the catalytic bed and assume that all the physical properties are independent of temperature and pressure. We assume that the surface coverage, θ (fraction of the adsorption capacity of the adsorbent, Q), is in equilibrium with the gaseous product concentration adjacent to the surface, c_i. The corresponding dimensionless mass and energy balances are

$$\frac{\epsilon}{\sigma}\frac{\partial x_A}{\partial \tau}+\frac{f}{Da}\frac{\partial x_A}{\partial \xi}-\frac{1}{\phi_m^2}\frac{\partial^2 x_A}{\partial \xi^2}+B(y)\cdot x_A=0 \quad (1)$$

$$\frac{\epsilon}{\sigma}\frac{\partial x_P}{\partial \tau}+\frac{f}{Da}\frac{\partial x_P}{\partial \xi}-\frac{1}{\phi_m^2}\frac{\partial^2 x_P}{\partial \xi^2}+\frac{M}{Da}\cdot(x_P-x_i)-B(y)\cdot x_A=0 \quad (2)$$

$$\frac{C}{\sigma}\frac{\partial \theta}{\partial \tau}-\frac{M}{Da}(x_P-x_i)=0 \quad (3)$$

$$\frac{Le}{\sigma}\frac{\partial y}{\partial \tau}-\frac{\beta_{\text{ads}}\cdot C}{\sigma}\frac{\partial \theta}{\partial \tau}+\frac{f}{Da}\frac{\partial y}{\partial \xi}-\frac{1}{\phi_h^2}\frac{\partial^2 y}{\partial \xi^2}-\beta\cdot B(y)\cdot x_A+\Delta\cdot(y-y_c)=0. \quad (4)$$

The flow-direction indicator f is equal to $1(-1)$ for flow from the left (right). Assuming that no product is present in the feed, the corresponding boundary conditions for a flow from left to right ($f=1$) are

$$\frac{Da}{\phi_m^2}\frac{\partial x_A}{\partial \xi}\bigg|_{\xi=0}=x_A|_{\xi=0}-1 \quad (5)$$

$$\frac{Da}{\phi_m^2}\frac{\partial x_P}{\partial \xi}\bigg|_{\xi=0}=x_P|_{\xi=0} \quad (6)$$

$$\frac{Da}{\phi_h^2}\frac{\partial y}{\partial \xi}\bigg|_{\xi=0}=y|_{\xi=0}-1 \quad (7)$$

$$\frac{\partial x_A}{\partial \xi}\bigg|_{\xi=1}=\frac{\partial x_P}{\partial \xi}\bigg|_{\xi=1}=\frac{\partial y}{\partial \xi}\bigg|_{\xi=1}=0. \quad (8)$$

The dimensionless state variables in the preceding equations are

$$x_A=\frac{c_A}{c_{A0}},\quad x_P=\frac{c_P}{c_{A0}},\quad x_i=\frac{c_i}{c_{A0}},\quad y=\frac{T}{T_0},\quad \tau=\frac{t}{t_c},\quad \xi=\frac{z}{L}. \quad (9)$$

The dimensionless groups are

$$\sigma=t_c\cdot k(T_0),\quad Le=\frac{(\rho c_p)_s}{(\rho c_p)_g}\cdot(1-\epsilon)+\epsilon,$$

$$Da=\frac{L\cdot K(T_0)}{u},\quad \gamma=\frac{E_\infty}{R\cdot T_0},\quad \phi_h^2=\frac{L^2\cdot k(T_0)\cdot(\rho c_p)_g}{\bar{\lambda}},$$

$$\phi_m^2=\frac{L^2\cdot k(T_0)}{\bar{D}},\quad \beta=\frac{(-\Delta H)\cdot c_{A0}}{(\rho c_p)_g\cdot T_0},\quad y_c=\frac{T_c}{T_0},$$

$$\Delta=\frac{u_W\cdot a_W}{(\rho c_p)_g\cdot k(T_0)},\quad \beta_{\text{ads}}=\beta\frac{(\Delta H_{\text{ads}})}{(-\Delta H)},\quad M=\frac{k_c\cdot a_v\cdot L}{u},$$

$$C=\frac{Q\cdot a_s}{c_{A0}},\quad B(y)=\frac{k_c\cdot a_v\cdot\exp[\gamma(1-1/y)]}{k_c\cdot a_v+k_\infty\exp(-\gamma/y)}, \quad (10)$$

where

$$k(T_0)=k_\infty\cdot\exp(-\gamma). \quad (11)$$

The effective heat conductivity $\bar{\lambda}$ satisfies the relation (Vortmeyer and Schaefer, 1974)

$$\bar{\lambda}=\frac{u^2(\rho c_p)_g^2}{ha_v}+(1-\epsilon)\lambda_s. \quad (12)$$

Common expressions of the adsorption equilibrium account for adsorption isotherms under stationary conditions. We develop here a relation adequate for a dynamic situation. When the long-range intermolecular forces are weak, the adsorption rate is a product of the rate of collision of molecules on the surface and the sticking coefficient. From the kinetic-gas theory one obtains (Masel, 1996)

$$r_{\text{ads}}=\frac{dc_{\text{ads}}}{dt}=\frac{s}{\sqrt{2\pi M_i RT}}p_i(1-\theta). \quad (13)$$

The value of the sticking probability s depends on the adsorbent and adsorbate as well as temperature, pressure, chemical potential, and other state parameters. We assume that it is a constant. Note that according to Eq. 13 the adsorption rate is not activated. The adsorption is activated if the repulsive forces between adsorbent and adsorbate are not negligible or if dissociation occurs. An apparent activation is possible, if diffusion processes are the rate-determining steps during the adsorption process.

The desorption is always an activated process, as the adsorption process is exothermic due to its negative entropy. If the adsorption is a nonactivated process, as in the present case, the activation energy of a simple desorption mechanism is the heat of adsorption. (The activation energy may be larger for a complicated mechanism, e.g., with multiple transition states.) We describe the desorption rate by

$$r_{\text{des}}=\frac{dc_{\text{ads}}}{dt}=-k_D\exp\left(-\frac{\Delta H_{\text{ads}}}{RT}\right)\cdot\theta. \quad (14)$$

The equilibrium surface coverage of the adsorbate is found by combining Eqs. 13 and 14

$$\theta=\frac{1}{K\exp\left(-\frac{\Delta H_{\text{ads}}}{RT}\right)\frac{\sqrt{T}}{p_i}+1}, \quad (15)$$

where

$$K=\frac{k_D\sqrt{2\pi M_i R}}{s}. \quad (16)$$

Table 1. Parameters Used in the Simulations

a_s	$1.3\cdot10^7$ m^2/m$^3_{\text{React}}$	k_c	0.023 m/s
a_v	1314.4 m^2/m$^3_{\text{React}}$	k_∞	1.815×10^6 s^{-1}
a_W	1.0 m^2/m$^3_{\text{React}}$	L	4.0 m
c_{A0}	0.5 mol/m^3	$T_0 = T_c$	323 K
$\overline{D}$	10^{-3} m^2/s	t_c	600 s
E_∞/R	8,328.6 K	u	0.8 m/s
h	0.025 kW/(m$^2\cdot$K)	ϵ	0.69
$-\Delta H$	62.44 kJ/mol	λ_s	1.26 W/(m$\cdot$K)
ΔH_{ads}	16.1 kJ/mol	$(\rho c_p)_g$	0.6244 kJ/(m$^3\cdot$K)
K	10,000 kg/(m$\cdot$s$^2\cdot$K$^{1/2}$)	$(\rho c_p)_s$	1,381.61 kJ/(m$^3\cdot$K)

Substituting $c_i = p_i/RT$ in Eq. 15 gives the equilibrium relation

$$\theta = \frac{x_i}{x_i + \left(\kappa/\sqrt{y}\right)\cdot\exp(-\gamma_{\text{des}}/y)}, \tag{17}$$

where

$$\gamma_{\text{des}} = \gamma\frac{\Delta H_{\text{ads}}}{E_\infty}, \qquad \kappa = \frac{K}{c_{A0}R\sqrt{T}_0}. \tag{18}$$

The analysis of the model features was conducted by computing bifurcation diagrams describing the dependence of a state of the system on a continuously changing parameter. In addition we computed the loci of various dynamic bifurcations, that is, of parameters at which a qualitative change in the dynamic features occurs. A detailed description of the method of calculating these bifurcations was given by Khinast et al. (1998). We provide a short description of the numerical scheme in the Appendix.

Operation of RFR with Product Adsorption

Extensive numerical simulations were carried out to determine the behavioral features of an RFR in which the product is adsorbed. The values of the parameters used in the simulations shown here are reported in Table 1. The semicycle (each cycle consists of two flow reversals) duration was 600 s in all the simulations reported here, except when otherwise indicated. The values of corresponding dimensionless groups are:

$$Le = 686.6, \qquad \sigma = 6.9\times10^{-3}, \qquad Da = 5.748\times10^{-5},$$
$$\phi_h^2 = 1.44\times10^{-2}, \qquad \phi_m^2 = 1.84\times10^{-1}, \qquad \beta = 0.155,$$
$$\beta_{\text{ads}} = 0.04, \qquad \gamma = 25.785, \qquad \gamma_{\text{ads}} = 5.995,$$
$$M = 1.51\times10^2, \qquad y_c = 1, \qquad \kappa = 1.338\times10^2. \tag{19}$$

Figure 1 shows the influence of the dimensionless adsorption capacity (C) on the temporal dimensionless exit product concentration (x_{pL}) over a semicycle. In all cases shown, a high-temperature zone exists within the reactor, leading to complete conversion of the reactant to the product. Due to product adsorption, however, the effluent product concentration is much lower than that of the inlet reactant (shown by the dotted line in Figure 1) following a flow-reversal. Eventually, this effluent product concentration increases and even

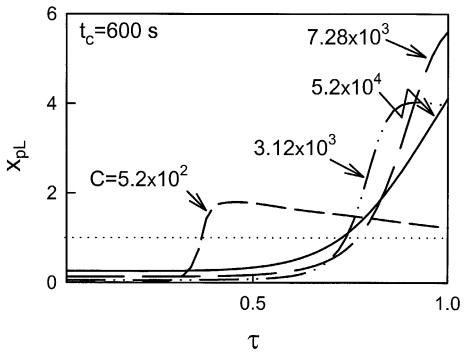

Figure 1. Impact of dimensionless product adsorption capacity, C, in an adiabatic RFR on the temporal product effluent concentration during a semicycle.

exceeds that of the dilute inlet reactant, as the total amount of effluent product in a semicycle must be equal to the total amount of converted reactant. For low adsorption capacities, the effluent product concentration attains a maximum value at a time shorter than that of a semicycle, and then decreases monotonically. For the case shown in Figure 1 the maximum effluent product concentration is attained at $\tau = 1$ for $C = 7.28\cdot10^3$. For all higher C values, the effluent product concentration is a monotonic increasing function of time. The temporal variation in the effluent product concentration can be used to our advantage to get the product with high concentration.

Figure 2 shows the spatiotemporal profiles of the dimensionless gas-phase product concentration in the RFR during a semicycle for two C values. The profile at $\tau = 0$ corresponds to the time at which the flow direction is switched from the left to the right (the arrow in Figure 2 indicates the flow direction during the semicycle). During the early stages of the semicycle the product concentration has a local maximum next to the inlet due to desorption of the product formed in the previous semicycle (see profile at $\tau = 0$). At relatively low adsorption capacities, such as the case shown in Figure 2 (top), a maximum in the product concentration tends also to form in the downstream section of the reactor. The concentration peak in the upstream section moves fast in the downstream direction and coalesces with the downstream peak. The maximum in the temporal effluent concentration is attained when this peak reaches the reactor end. After that the effluent concentration decreases with time.

An important parameter affecting the behavior of the RFR is the ratio between the amount of product adsorbed in the bed to that generated during a semicycle. When this ratio is large, which occurs at high C values, the rate of migration of the peak product concentration may be slowed down so that it does not reach the reactor end during the semicycle (Figure 2, bottom). This decreases the peak effluent product concentration at high C (Figure 1). For the case shown in the bottom of Figure 2 the amount of product adsorbed in the bed is about 100 times that which is generated by the reaction during a semicycle. For adsorption capacities exceeding that corresponding to Figure 2 (bottom), the RFR behavior becomes essentially independent of the adsorption capacity.

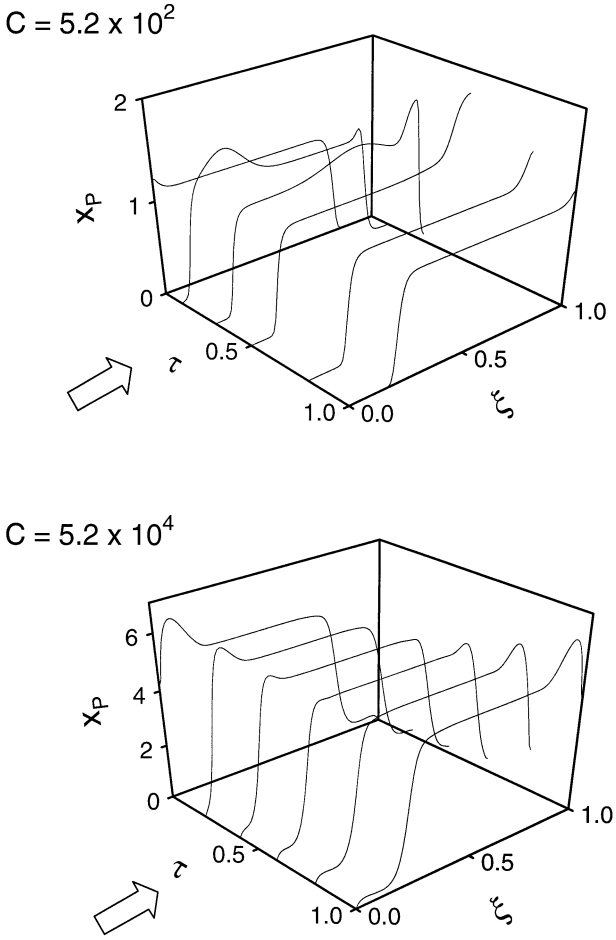

Figure 2. Temporal dimensionless product concentration profiles in an adiabatic RFR during a semicycle of a symmetric period-1 state.

This asymptotic behavior is due to the very large amount of adsorbed product in the bed, so that the desorption and adsorption of the product during the semicycle cause only minor perturbations to the adsorbed product profile.

An increase in the wall cooling of an RFR decreases the size of the hot zone in the reactor and increases the size of the cold regions around it (Khinast et al., 1998). The increase in the cold regions increases the product adsorption and slows down the movement of the product in the bed. This increases the fraction of the semicycle time during which the product effluent is low. This, in turn, increases the maximum in the temporal effluent concentration. This is illustrated by Figure 3, which shows the dependence of the temporal profiles of the dimensionless effluent product concentration on the cooling capacity, Δ.

Figure 4 describes the influence of the semicycle time, t_c, on the fraction of the switching time (τ_{xpL}) at which the effluent product concentration reaches a specified fraction of the feed concentration. At larger times the effluent concentration exceeds this value. The separation among curves for different values of effluent product concentration in Figure 4 are indicative of the temporal rate of increase in the product effluent concentration after the initial delay. Small separa-

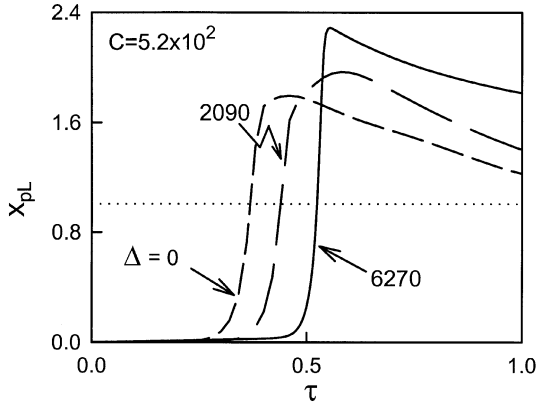

Figure 3. Influence of the cooling capacity, Δ, on the temporal effluent product concentration during a semicycle.

tion at a particular t_c implies a sharp increase in the exit product concentration. This shows the advantage of operation with large semicycle time. Figure 4 (top) indicates that for low adsorption capacities and short semicycle time, τ_{xpL} decreases monotonically with t_c. On the other hand, for high adsorption capacities and short semicycle times (Figure 4, bottom), τ_{xpL} increases monotonically with t_c. In both cases

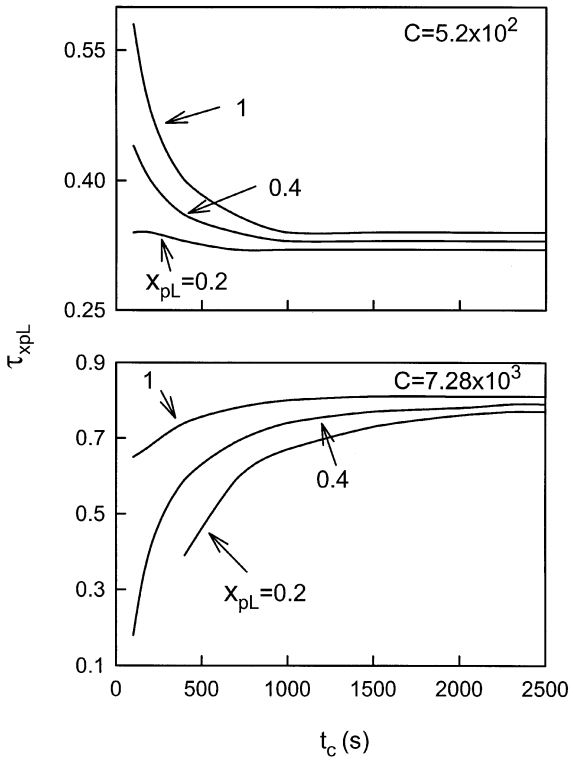

Figure 4. Impact of the switching time on the fraction of the semicycle time, τ_{xpL}, during which the ratio of effluent product concentration to feed reactant concentration, x_{pL}, is smaller than a specified value for an adiabatic RFR.

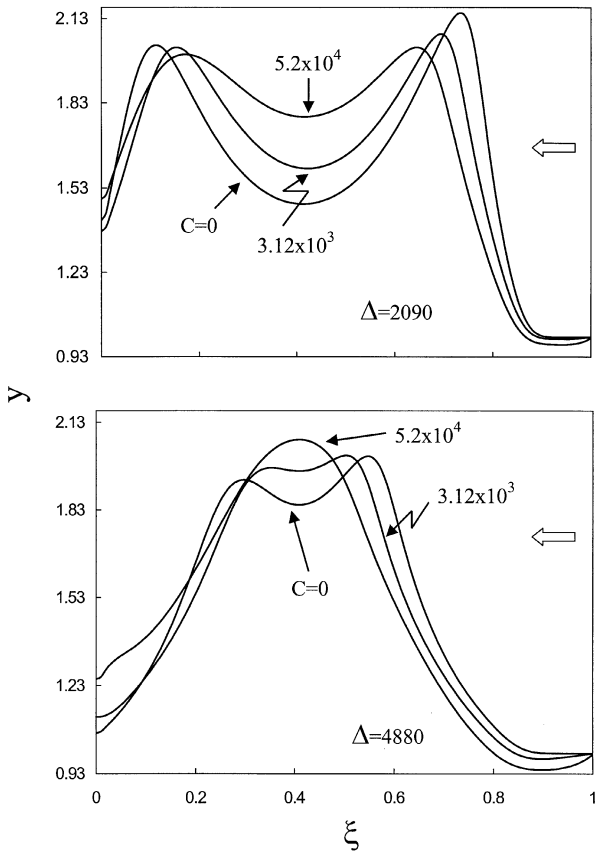

Figure 5. Influence of the dimensionless product adsorption capacity, C, on the temperature profiles of symmetric period-1 states at the end of a leftwards flow semicycle.

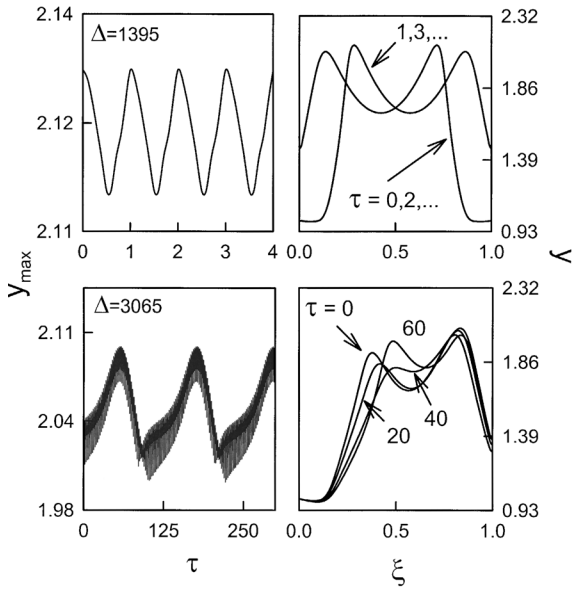

Figure 6. Time series of the dimensionless maximum RFR temperature, y_{max}, and corresponding temporal temperature profiles for a symmetric period-1 and a quasi-periodic state: $C = 3.12 \times 10^3$.

the curves reach an asymptotic value for high semicycle times. This behavior is due to the fact that for sufficiently high t_c the temperature and concentration front velocities in the RFR attain an asymptotic value. An increase in the semicycle time decreases the size of the hot zone and this increases the time, following a flow reversal, for the effluent concentration to reach the specified value. As C is increased, the corresponding asymptotic values of τ_{xpL} increase.

Under heat losses and/or cooling the temperature profile of the RFR tends to have two local maxima. Figure 5 (top) shows several dimensionless temperature profiles when the flow is switched from the left to the right for two values of Δ. As C is increased, the maximum bed temperature and the size of the cold zone (the distance between the two maxima in the temperature profile) decrease. The reason is that an increase in C increases the rate of desorption in the upstream section of the reactor and at the moving front in the downstream section of the reactor. This desorption decreases the maximum temperature of both temperature peaks. The increased adsorption of the product in the region between these two peaks increases the temperature in that region. In the case shown in Figure 5 (top) the temperature profiles became essentially independent of the adsorption capacity for C values exceeding 5.2×10^4. In the higher cooling capacity case shown in Figure 5 (bottom) the increase in the adsorption capacity causes the temperature maxima to move toward each other and eventually coalesce at high adsorption capacity of 5.2×10^4. Figure 5 shows that at high C, the high rate of desorption decreases the temperature near the reactor entrance below the feed temperature.

The RFR usually attains a symmetric period-1 state so that its profile upon a flow reversal is a mirror image of that at the following flow reversal. However, under cooling and relatively short semicycle periods the RFR may attain rather complex dynamic states, such as asymmetric states, period-n motion, quasi-periodic, and even chaotic motion (Khinast et al., 1998; Rehacek et al., 1998). Similar complex dynamic states may be attained when the adsorption capacity is not too large. Figure 6 shows the shift from a period-1 state to a quasi-periodic state as the cooling is increased from $\Delta = 1395$ to $\Delta = 3065$ for a dimensionless adsorption capacity of 3.12×10^3. The left column in Figure 6 shows the time series of the dimensionless maximum reactor temperature. The right column shows the corresponding dimensionless temperature profiles. Inspection of the time profiles of the quasi-periodic state indicates that the reactor returns approximately (but not exactly) to its original state after about 120 flow reversals.

The impact of the wall cooling on the dynamics of the RFR is efficiently illustrated by a bifurcation diagram, such as Figure 7, that describes the dependence of the dimensionless maximum RFR temperature on Δ. This diagram is qualitatively similar to one obtained by Khinast et al. (1998) for an RFR in which no product adsorption occurs. Ignited states exist in addition to extinguished states for values of Δ smaller than that of the limit point (L-S) of the branch of symmetric period-1 states. For higher Δ only extinguished states exist. Most of the ignited states are stable symmetric period-1 states. At low values of Δ the temperature profiles of the symmetric

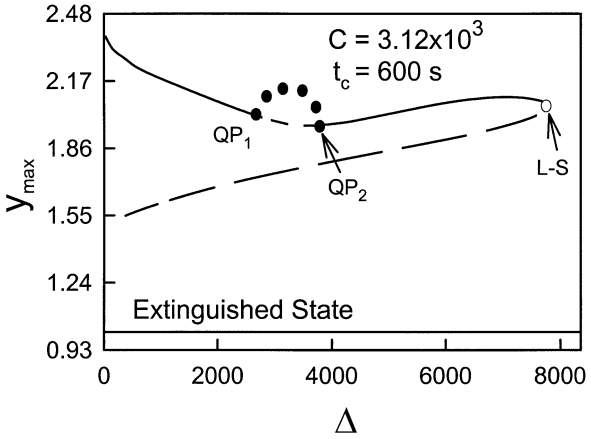

Figure 7. Bifurcation diagram of the dimensionless maximum temperature, y_{max}, vs. the cooling capacity, Δ.

QP = quasi-periodic bifurcation; L-S = limit point of the symmetric period-1 states; solid circle = quasi-periodic states; solid line = stable symmetric period-1 states; dashed line = unstable symmetric period-1 states.

period-1 states have two maxima. However, the temperature profiles of the symmetric period-1 states close to the limit point have only one maximum. At intermediate Δ two bifurcations to quasi-periodic states occur (QP). Between these two bifurcation points the symmetric state is unstable and the reactor attains quasi-periodic motion. These states are indicated by the solid circles in Figure 7.

The space-time dependence of the temperature within the reactor provides important insight into the dynamic behavior. Figure 8 shows this dependence for three different values of Δ. At Δ = 1395, the reactor attains a symmetric period-1 state with two temperature maxima moving back and forth in each cycle, leading to a mirror symmetry over successive semicycles. At the higher Δ value of 6270 a period-1 motion still exists. However, the corresponding temperature profile has only one maximum at the center of the reactor. At the intermediate Δ value of 3065 the reactor attains a quasi-periodic state, which does not exhibit mirror symmetry. Note that the space-time diagram of the quasi-periodic state is shown over a period of 300 semicycles, while those for the period-1 motions are over a period of 4 semicycles.

The bifurcation diagram in Figure 7 clearly shows that an ignited state can exist only when the bifurcation variable is smaller than its value at the limit point of the branch of period-1 states. Figure 9 describes the dependence of the semicycle time at the limit point on the value of the dimensionless adsorption capacity for an adiabatic RFR. Increasing C decreases the semicycle time at which the limit point occurs and causes the reactor to extinguish at shorter semicycle times. This occurs because the increased product desorption decreases the maximum temperature and increases the convective heat removal from the reactor. The cycle time corresponding to the limit point attains an asymptotic value at high C.

It is important to know the set of operating conditions at which the RFR exhibits complex dynamic features, as one usually wants to avoid operating in that region. This information is best presented through bifurcation maps, which show the parameter regions in which complex dynamic behavior is attained. Figure 10 is such a bifurcation map, constructed in

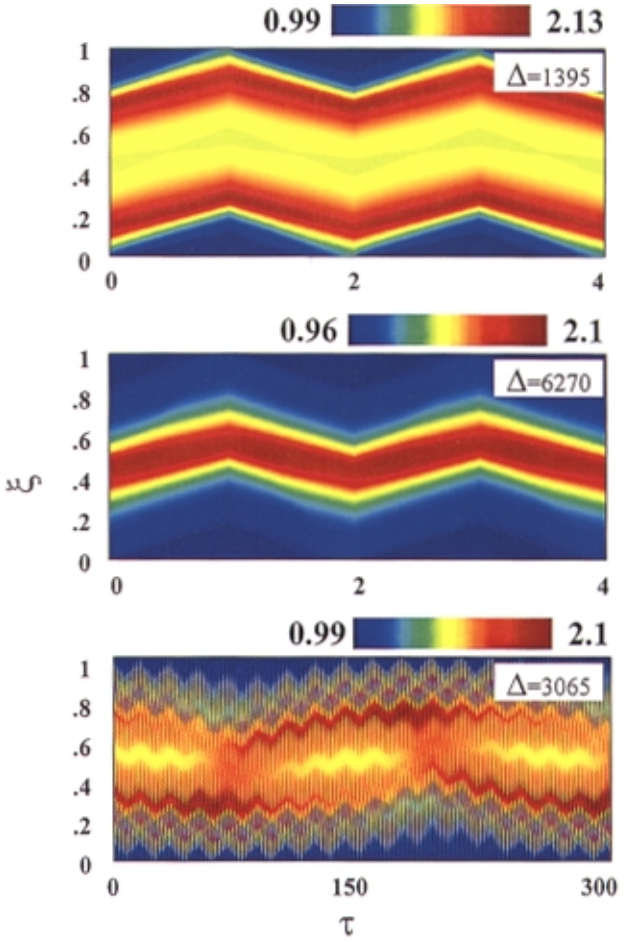

Figure 8. Influence of the cooling capacity, Δ, on the space-time temperature: $C = 3.12 \times 10^3$.

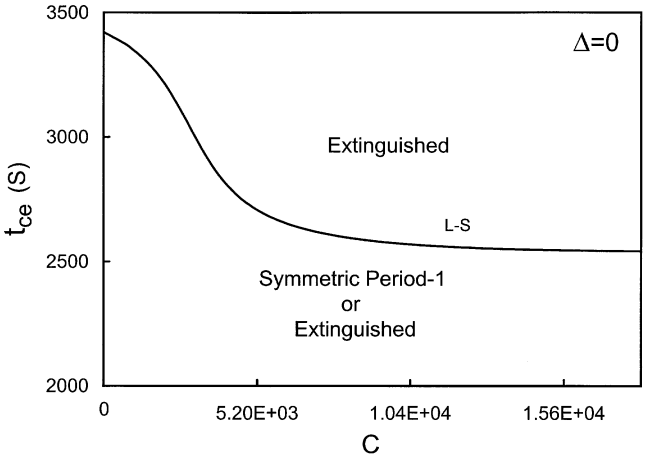

Figure 9. Influence of the dimensionless product adsorption capacity, C, on the maximum possible switching time, t_{ce}, for which an ignited state exists: Δ = 0.

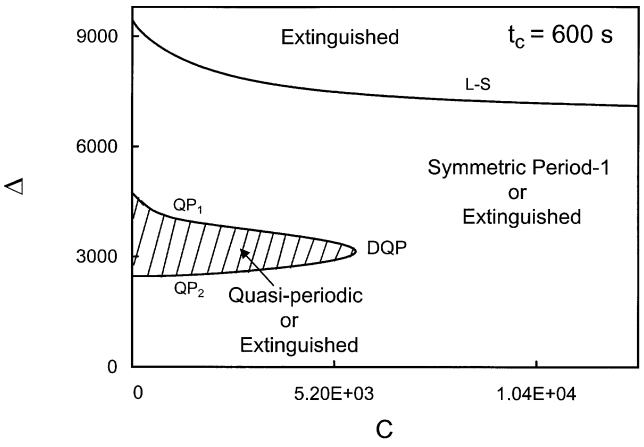

Figure 10. Map of regions with qualitatively different dynamic behavior.

L-S = limit point of the symmetric period-1 states; QP = quasi-periodic bifurcation; DQP = degenerate quasi-periodic bifurcation.

the plane of the cooling capacity, Δ, and dimensionless adsorption capacity, C. Ignited states exist in addition to extinguished states in the region below the locus of the limit point of the symmetric period-1 states (L-S). The figure shows that the value of Δ at the limit point decreases with increasing C, and eventually reaches an asymptotic value at high C. This decrease in the value of Δ occurs because the heat released by the adsorption of the product at the cold downstream section of the reactor is convected away by the outgoing stream. This heat loss increases with increasing C values, causing the reactor extinction at lower Δ.

Figure 10 shows that the RFR exhibits quasi-periodic states in a region bounded by the loci of the quasi-periodic bifurcations (QP_1 and QP_2) that coalesce at a *degenerate quasi-periodic bifurcation* (DQP), which is a singular point of codimension-2. In a quasi-periodic state the position and magnitude of the two maxima in the temperature profile change slowly between successive cycles. An increase in C dampens the amplitude of these motions as an increase (decrease) in the temperature maximum in the RFR will increase product desorption (adsorption), which in turn, partially counteracts the temperature change. Figure 11 illustrates this damping in magnitude of the amplitude of temperature oscillations as the value of C is increased. Thus, the RFR does not attain any quasi-periodic states as C exceeds a critical value (5.7×10^3 in this case). It should be pointed out that some very narrow parameter regions with other dynamic features may exist close to the QP bifurcation. These are, however, too small to be shown on the map, and are mainly of academic interest.

Figure 12 shows three space-time figures illustrating the impact of the adsorption capacity on the quasi-periodic motion of the RFR. When no product adsorption occurs ($C = 0$), the two temperature maxima move in opposite directions from one side of the reactor to the other. When one of these maxima gets close to a reactor end, the heat losses by the wall cooling and convection cause its extinction. When one maximum extinguishes, the second maximum splits into two pulses moving in opposite directions (behavior similar to backfiring). This temperature pulse motion is quite similar to that of the

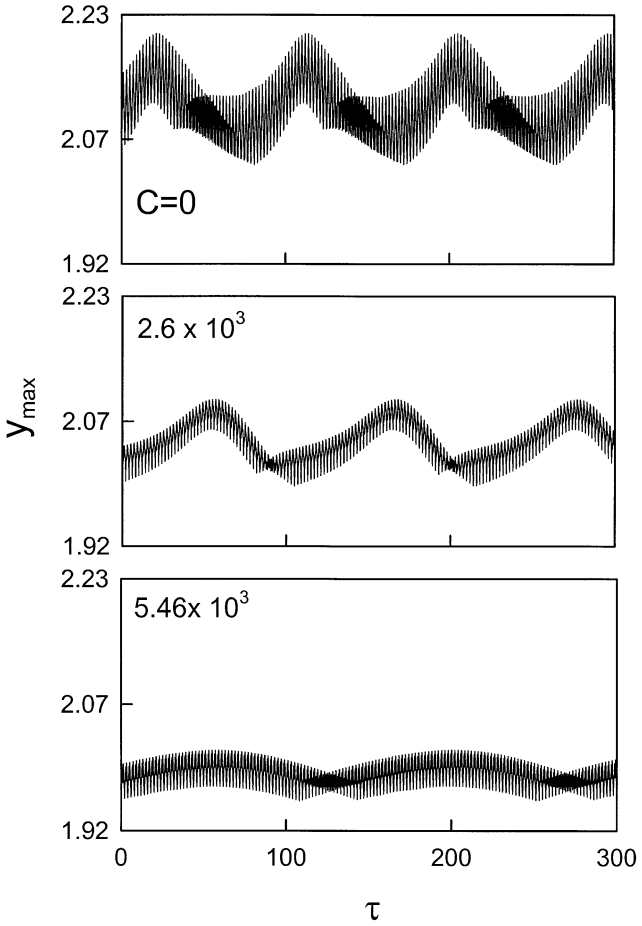

Figure 11. Influence of the dimensionless adsorption capacity, C, on the quasi-periodic time series of the dimensionless maximum RFR temperature, y_{max}: $\Delta = 3205$.

symmetric period-1 state observed in cooled countercurrent flow reactor by Garg and Luss (2001). The space-time figure for $C = 2.6\times10^3$ indicates that the increase in adsorption capacity decreases the reactor maximum temperature and the range of motion of the high-temperature pulses. When C is increased to 5.46×10^3, the motion of the two pulses is strongly limited and its time average is very similar to that of a period-1 motion with two temperature peaks.

One of the surprising features of the dynamics of the RFR with product adsorption is that for some parameter values three stable, qualitatively different quasi-periodic states exist for the same operating conditions. Figure 13 shows the Poincaré maps of three such states attained for the same set of parameters. These maps show the dependence of averaged difference between the dimensionless temperatures in the right and left half of the RFR

$$\Delta y_{av}[n] = 2\left[\int_0^{1/2} y[n,\xi]\,d\xi - \int_{1/2}^{1} y[n,\xi]\,d\xi\right], \qquad n = 1,2,3,\ldots \quad (20)$$

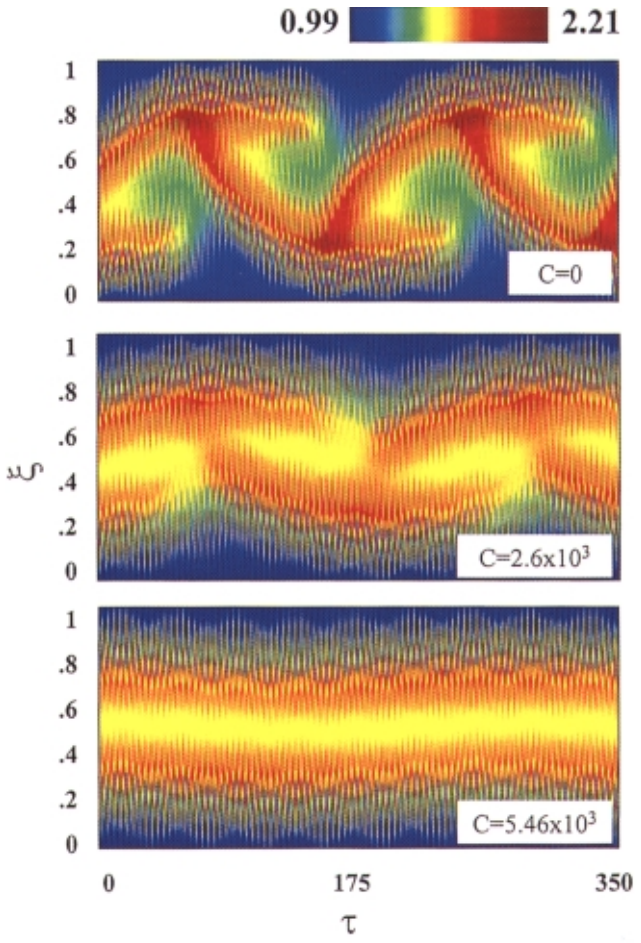

Figure 12. Influence of the adsorption capacity on the quasi-periodic space-time temperature motion: $\Delta = 3205$.

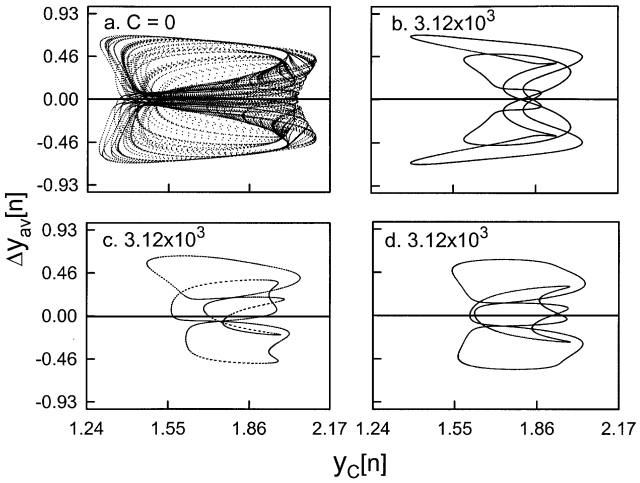

Figure 13. (a) Poincaré map of a chaotic state, and (b, c, and d) three qualitatively different quasi-periodic states: $u = 0.6$ m/s, $t_c = 300$ s, and $\Delta = 3{,}900$.

on $y_c[n]$, the dimensionless temperature at the reactor center after n flow reversals. The initial conditions determine which of the three is attained. Previous studies by Rehacek et al. (1998) found that an RFR can attain two stable period-n states, with different n. However, this is the first report of the existence of three quasi-periodic states in an RFR. Since no theoretical guidance exists on how to find all the possible states with complex dynamics, we cannot rule out the possibility that an even larger number of states with qualitatively different dynamic features exist.

We used numerical dynamic simulations to find the range of parameter values for which the branches of the complex states exist (Figure 14). We were not able to determine which bifurcations lead to the emergence and disappearance of the various branches, or how these branches are connected. Figure 14 shows that a chaotic state exists when the product adsorption is small or does not occur. The Poincaré map of such a chaotic state is shown in Figure 13. A branch of quasi-periodic states (type b in Figure 13) emerges at $C = 1 \times 10^3$ and is transformed at $C = 3.48 \times 10^4$ to a symmetric period-1 state (QP-S bifurcation). The Poincaré maps of the quasi-periodic states of type b are symmetric about the abscissa. At $C = 2.9 \times 10^3$ the chaotic state bifurcates and is

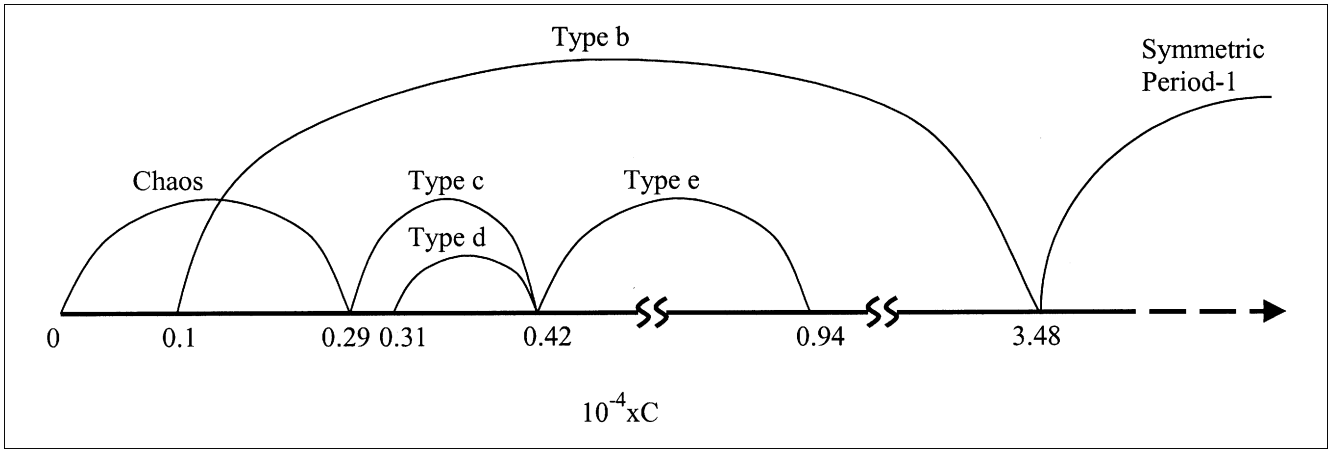

Figure 14. The range of the adsorption capacities for which various branches of states shown in Figure 13 exist.

transformed to a quasi-periodic state (type c). At $C = 3.1 \times 10^3$ an additional branch of quasi-periodic states emerges (type d). Poincaré maps of the quasi-periodic states of type c and d are shown in Figures 13c and 13d, respectively. Note that the Poincaré maps of both these states are asymmetric around the abscissa. The existence of type-c or -d states implies the existence of two additional quasi-periodic states, the Poincaré maps of which are mirror images of those of type c and d. At $C = 4.2 \times 10^3$ branches c and d coalesce into a quasi-periodic state (type e) that has a symmetric Poincaré map. This branch is annihilated at $C = 9.4 \times 10^3$.

Figure 14 indicates that there is a bounded range of C value in which either a chaotic or a quasi-periodic state (type b) is obtained, depending on the initial conditions. In addition, there are ranges of adsorption capacities in which either one (type b), two (types b and either c or e), or even three (types b, c, and d) different quasi-periodic motions exist. When more than one stable quasi-periodic states exist, the initial conditions determine which is obtained.

Discussion and Conclusions

The product adsorption in an RFR in which the reactant conversion is high may lead to large variations in the temporal effluent concentration. Using a dilute reactant feed, the adsorbed product concentration is lower than that of the reactant following a flow reversal. However, it later exceeds that of the reactant. The effluent product concentration can be increased by increasing either the dimensionless adsorption capacity, C, or the cooling capacity, Δ. In order to maximize the increase in the effluent product concentration, it is usually desirable to operate the RFR with long switching times. This large temporal change in the product concentration can be exploited to obtain an effluent with a high product concentration.

The product adsorption increases the convective heat loss from the RFR by the effluent. This decreases the range of cycle times for which the reactor attains an ignited state. Thus, product adsorption may necessitate shortening the switching time in order to maintain an RFR in an ignited state. This impact of the heat loss can be decreased by placing an inert, nonadsorbing material at both ends of the reactor to recover the lost heat. This mode of operation was not considered in any of the examples presented here.

The map in Figure 10 shows that the range of Δ for which an RFR exhibits quasi-periodic states decreases with an increase in C. In general, product adsorption reduces the region of operating conditions in which states with complex dynamics exist under cooling, which may destabilize the symmetric period-1 states. While the existence of states with complex dynamics is of academic interest, one wants to keep them from occurring in practice. We conclude that product adsorption increases the robustness of the RFR operation.

Rehacek et al. (1998) have shown that under cooling an RFR can attain two different stable period-n states. We found that under product adsorption the RFR can have three stable states with different complex dynamics. This is the first finding of such behavior in a chemical reactor. As there is no systematic procedure for finding all the possible complex states, we cannot guarantee that we found all the possible ones. Unfortunately, we were unable to determine the bifurcations leading to the appearance or annihilation of the various branches of solutions. It would be highly interesting to determine these and the relations among the various branches of these complex states.

Acknowledgments

The authors gratefully acknowledge the financial support by the ACS-PRF and the ExxonMobil Foundation. They are also thankful to Dr. Johannes Khinast for many helpful discussions.

Notation

a_s = specific internal particle surface area, m^2/m^3_{React}
a_v = specific external particle surface area, m^2/m^3_{React}
a_W = specific reactor wall surface area, m^2/m^3_{React}
$B(y)$ = temperature dependence of reaction rate
c = concentration, mol/m^3
c_{A0} = feed reactant concentration, mol/m^3
c_{ads} = concentration of product adsorbed on the support, mol/m^2
C = dimensionless adsorption capacity
$\overline{D}$ = effective gas-diffusion coefficient, m^2/s
Da = Damköhler number
E_∞ = activation energy, J/mol
h = heat-transfer coefficient between fluid and catalyst, $W/(m^2 \cdot K)$
$-\Delta H$ = heat of reaction, J/mol
ΔH_{ads} = heat of adsorption, J/mol
k_c = mass-transfer coefficient, m/s
k_D = desorption frequency factor, $mol/(m^2 \cdot s)$
k_∞ = frequency factor, 1/s
$k(T_0)$ = reaction rate constant at temperature T_0, 1/s
K = adsorption constant, $kg/(m \cdot s^2 \cdot K^{1/2})$
L = reactor length, m
Le = Lewis number
M = dimensionless mass-transfer parameter
M_i = molar mass, kg/mol
p_i = partial pressure, Pa
Q = adsorption capacity, mol/m^2_{Surf}
r = rate of reaction, $mol/(s \cdot m^3)$
r_{ads} = rate of adsorption, $mol/(m^2 \cdot s)$
r_{des} = rate of desorption, $mol/(m^2 \cdot s)$
R = universal gas constant, $J/(mol \cdot K)$
s = sticking probability
t = time, s
t_c = half-cycle time (one flow reversal), s
t_{ce} = maximum flow period before which the RFR extinguishes, s
T = temperature, K
u = superficial velocity, m/s
u_W = wall heat-transfer coefficient, $W/(m^2 \cdot K)$
x = dimensionless concentration
x_{pL} = dimensionless exit gas-phase product concentration
y = dimensionless temperature
z = axial position, m

Greek letters

β = dimensionless adiabatic temperature rise for reaction
β_{ads} = dimensionless adiabatic temperature rise for adsorption
Δ = cooling capacity
ϵ = void fraction
γ = dimensionless activation energy
γ_{des} = dimensionless activation energy for desorption
κ = dimensionless adsorption constant
$\overline{\lambda}$ = effective thermal conductivity, $W/(m \cdot K)$
λ_s = solid thermal conductivity, $W/(m \cdot K)$
ξ = dimensionless axial position
ρc_P = volumetric heat capacity, $J/(m^3 \cdot K)$
σ = dimensionless reference time
τ = dimensionless time
τ_{xpL} = dimensionless time at which exit product concentration reaches a particular value

θ = fraction of adsorption sites occupied
ϕ_h^2 = heat-transport modulus
ϕ_m^2 = mass-transport modulus

Indices

A = gas-phase reactant
c = coolant
g = gas phase
i = gas-phase product in equilibrium with the adsorbed phase
P = gas-phase product
s = solid phase
0 = feed

Literature Cited

Agar, D. W., and W. Ruppel, "Extended Reactor Concept for Dynamic $DeNO_x$ Design," *Chem. Eng. Sci.*, **43**, 2073 (1988).

Boreskov, G. K., and Yu. Sh. Matros, "Unsteady-State Performance of Heterogeneous Catalytic Reactions," *Catal. Rev. Sci. Eng.*, **25**, 551 (1983).

Broyden, C. G., "A Class of Methods for Solving Nonlinear Simultaneous Equations," *Math. Comput.*, **19**, 577 (1965).

Bunimovich, G. A., N. V. Vernikovskaya, V. O. Strots, B. S. Balzhinimaev, and Yu. Sh. Matros, "SO_2 Oxidation in a Reverse-Flow Reactor: Influence of a Vanadium Catalyst Dynamic Properties," *Chem. Eng. Sci.*, **50**, 565 (1995).

Deuflhard, P., E. Hairer, and J. Zugck, "One-Step and Extrapolation Methods for Differential-Algebraic Systems," *Numer. Math.*, **51**, 501 (1987).

Garg, R., and D. Luss, "Dynamic Bifurcations and Features of a Cooled Countercurrent Flow Reactor," *Chem. Eng. Sci.*, **56**, 3719 (2001).

Gupta, V. K., and S. K. Bhatia, "Solution of Cyclic Profiles in Catalytic Reactor Operation with Periodic Flow Reversal," *Comput. Chem. Eng.*, **15**, 229 (1991).

Keller, H. B., "Numerical Solutions of Bifurcation and Nonlinear Eigenvalue Problems," *Applications of Bifurcation Theory*, P. H. Rabinowitz, ed., Academic Press, New York, p. 359 (1977).

Khinast, J., A. Gurumoorthy, and D. Luss, "Complex Dynamic Features of a Cooled Reverse-Flow Reactor," *AIChE J.*, **44**, 1128 (1998).

Khinast, J., Y. O. Jeong, and D. Luss, "Dependence of Cooled Reverse-Flow Reactor Dynamics on Reactor Model," *AIChE J.*, **45**, 299 (1999).

Kolios, G., and G. Eigenberger, "Styrene Synthesis in a Reverse-Flow Reactor," *Chem. Eng. Sci.*, **54**, 2637 (1999).

Kolios, G., J. Frauhammer, and G. Eigenberger, "Autothermal Fixed-Bed Reactor Concepts," *Chem. Eng. Sci.*, **55**, 5945 (2000).

Masel, R. I., *Principles of Adsorption and Reaction on Solid Surfaces*, Wiley, New York (1996).

Matros, Yu. Sh., and G. A. Bunimovich, "Reverse-Flow Operation in Fixed Bed Catalytic Reactors," *Catal. Rev. Sci. Eng.*, **38**, 1 (1996).

Nieken, U., G. Kolios, and G. Eigenberger, "Fixed-Bed Reactors with Periodic Flow Reversals: Experimental Results for Catalytic Combustion," *Catal. Today*, **20**, 335 (1994).

Noskov, A., L. Bobrova, G. A. Bunimovich, O. Goldman, A. Zagoruiko, and Yu. Sh. Matros, "Application of the Nonstationary State of a Catalyst Surface for Gas Purification from Toxic Impurities," *Catal. Today*, **27**, 315 (1996).

Rehacek, J., M. Kubicek, and M. Marek, "Periodic, Quasiperiodic and Chaotic Spatiotemporal Patterns in a Tubular Catalytic Reactor with Periodic Flow Reversal," *Comput. Chem. Eng.*, **22**, 283 (1998).

Snyder, J. D., and B. Subramaniam, "A Novel Reverse Flow Strategy for Ethylbenzene Dehydrogenation in a Packed-Bed Reactor," *Chem. Eng. Sci.*, **49**, 5584 (1994).

Snyder, J. D., and B. Subramaniam, "Numerical Simulation of a Reverse-Flow NO_x-SCR Reactor with Side-Stream Ammonia Addition," *Chem. Eng. Sci.*, **53**, 727 (1998).

van de Beld, B., R. A. Borman, O. R. Derkx, B. A. A. van Woezik, and K. R. Westerterp, "Removal of Volatile Organic Compounds from Polluted Air in a Reverse Flow Reactor: An Experimental Study," *Ind. Eng. Chem. Res.*, **33**, 2946 (1994).

van de Beld, B., "Air Purification by Catalytic Oxidation in an Adiabatic Packed-Bed Reactor with Periodic Flow Reversal," PhD Thesis, Univ. of Twente, Enschede, The Netherlands (1995).

Vortmeyer, D., and R. J. Schaefer, "Equivalence of One- and Two-Phase Models for Heat Transfer Processes in Packed Beds: One Dimensional Theory," *Chem. Eng. Sci.*, **29**, 485 (1974).

Appendix: Construction of Bifurcation Diagrams

The bifurcation diagrams and maps were constructed by the continuation method described in detail by Khinast et al. (1998). Here we briefly describe the application of that procedure to our problem. The set of the model ODEs (Eqs. 1–4) is solved to find a symmetric period-1 state by the method of solving the temporal boundary condition that was proposed by Gupta and Bhatia (1991):

$$\boldsymbol{F}^s = \boldsymbol{g}(\tau = 0) - \tilde{\boldsymbol{g}}(\tau = 1) = 0. \tag{A1}$$

Here $\boldsymbol{g}$ is a vector of spatially discretized state variables, and the tilde denotes mirror reflection, that is, it maps ξ into $1-\xi$.

The stability of a symmetric periodic state is determined by finding the eigenvalue spectrum of the monodromy matrix, $\boldsymbol{M}^s$, for a semicycle

$$\boldsymbol{M}^s = \left\{m_{i,j}^s\right\} = \left\{\frac{\partial \tilde{g}_i(\tau = 1)}{\partial g_j(\tau = 0)}\right\}. \tag{A2}$$

A periodic state is stable if all the eigenvalues of the monodromy matrix lie within a unit circle in the complex plane, otherwise it's unstable. At the limit point of a symmetric state, one eigenvalue of $\boldsymbol{M}^s$ crosses the unit circle at $\mu = +1$. A symmetric state undergoes a symmetry loss bifurcation when $\mu = -1$ is an eigenvalue of $\boldsymbol{M}^s$. A bifurcation from a periodic state to a quasi-periodic solution occurs when a complex-conjugate pair of eigenvalues of $\boldsymbol{M}^s$ crosses the unit circle.

Khinast et al. (1998) showed that at a bifurcation from symmetric period-1 states

$$\mu \boldsymbol{v}_0 = \tilde{\boldsymbol{v}}(\tau = 1) \tag{A3}$$

where $\boldsymbol{v}_0$ is the eigenvector of the Jacobian of the residual functions $\boldsymbol{F}^s$. The different bifurcations can be found by solving Eqs. 1–4 along with Eq. A3 for the value of μ, depending on the bifurcation of interest. The vector $\boldsymbol{v}(\tau = 1)$ (where $\boldsymbol{v} = [v_{x_A} \;\; v_{x_P} \;\; v_\theta \;\; v_y]$) is the solution of the linearized model equations integrated over a semicycle, that is, the solution of

$$\frac{\epsilon}{\sigma}\frac{\partial v_{x_A}}{\partial \tau} + \frac{f}{Da}\frac{\partial v_{x_A}}{\partial \xi} - \frac{1}{\phi_m^2}\frac{\partial^2 v_{x_A}}{\partial \xi^2} + B(y)\cdot v_{x_A} + x_A \cdot \frac{\partial B(y)}{\partial y}\cdot v_y = 0 \tag{A4}$$

$$\frac{\epsilon}{\sigma}\frac{\partial v_{x_P}}{\partial \tau} + \frac{f}{Da}\frac{\partial v_{x_P}}{\partial \xi} - \frac{1}{\phi_m^2}\frac{\partial^2 v_{x_P}}{\partial \xi^2} + \frac{M}{Da}(v_{x_p} - v_{x_i}) - B(y)\cdot v_{x_A} - x_A \cdot \frac{\partial B(y)}{\partial y}\cdot v_y = 0 \tag{A5}$$

$$\frac{C}{\sigma}\frac{\partial v_\theta}{\partial \tau} - \frac{M}{Da}(v_{x_P} - v_{x_i}) = 0 \tag{A6}$$

$$\frac{Le}{\sigma}\frac{\partial v_y}{\partial \tau} - \frac{\beta_{\text{ads}}\cdot C}{\sigma}\frac{\partial v_\theta}{\partial \tau} + \frac{f}{Da}\frac{\partial v_y}{\partial \xi} - \frac{1}{\phi_h^2}\frac{\partial^2 v_y}{\partial \xi^2} - \beta\cdot B(y)\cdot v_{x_A} - \beta\cdot x_A\cdot\frac{\partial B(y)}{\partial y}v_y + \Delta\cdot v_y = 0, \quad \text{(A7)}$$

subject to the spatial boundary conditions

$$\frac{Da}{\phi_m^2}\frac{\partial v_{x_A}}{\partial \xi}\bigg|_{\xi=0} = v_{x_A}|_{\xi=0} \quad \text{(A8)}$$

$$\frac{Da}{\phi_m^2}\frac{\partial v_{x_P}}{\partial \xi}\bigg|_{\xi=0} = v_{x_P}|_{\xi=0} \quad \text{(A9)}$$

$$\frac{Da}{\phi_h^2}\frac{\partial v_y}{\partial \xi}\bigg|_{\xi=0} = v_y|_{\xi=0} \quad \text{(A10)}$$

$$\frac{\partial v_{x_A}}{\partial \xi}\bigg|_{\xi=1} = \frac{\partial v_{x_P}}{\partial x}\bigg|_{\xi=1} = \frac{\partial v_y}{\partial x}\bigg|_{\xi=1} = 0, \quad \text{(A11)}$$

where

$$\frac{\partial B(y)}{\partial y} = \frac{a_v k_c}{\left[a_v k_c + k_\infty \exp(-\gamma/y)\right]}\cdot\frac{\gamma}{y^2}\cdot B(y), \quad \text{(A12)}$$

and the initial condition

$$\boldsymbol{v}(\tau = 0) = \boldsymbol{v}_0. \quad \text{(A13)}$$

Since an eigenvector is defined only up to a multiplicative constant, we set the norm of the vector to be an arbitrary constant. This condition serves as an additional defining equation.

For the numerical calculations the PDE system is discretized on an equidistant grid (Method of Lines), and the resulting system of ordinary differential equations (ODE system) is solved by a standard implicit solver, LIMEX (Deuflhard et al., 1987), for stiff initial-value problems. The spatial boundary values are included in the discretized function. An internal test has shown that a grid of 101 points provides sufficient accuracy at a reasonable computational effort. A shooting algorithm is employed to solve the boundary-value problem in time. Broyden's quasi-Newton-algorithm (Broyden, 1965) is used for the resulting root-finding problem.

Calculation of loci of different bifurcations was done using pseudo-arc-length continuation technique (Keller, 1977). In this method the solution of one step is extrapolated to find an initial guess for the next step, and the corresponding quasi-Newton-matrix is used as the initial value for the next Broyden iteration. This procedure is significantly less expensive than the calculation of the monodromy matrix and the calculation of its eigenvalues at every step. However, the Monodromy matrix and the Floquet multipliers were calculated for some steps in order to check the validity of the stability predictions.

Manuscript received Mar. 29, 2001, and revision received July 20, 2001.